Exceptional Points and Skin Modes in Non-Hermitian Metabeams

Runcheng Cai, Yabin Jin, Yong Li, Timon Rabczuk, Yan Pennec, Bahram Djafari-Rouhani, Xiaoying Zhuang

Exceptional Points and Skin Modes in Non-Hermitian Metabeams

Runcheng Cai,[1] Yabin Jin,[2,*] Yong Li,[3] Timon Rabczuk,[4] Yan Pennec,[5] Bahram Djafari-Rouhani,[5] and Xiaoying Zhuang[1,6,†]

[1] *Department of Geotechnical Engineering, College of Civil Engineering, Tongji University, 200092 Shanghai, China*

[2] *School of Aerospace Engineering and Applied Mechanics, Tongji University, 200092 Shanghai, China*

[3] *Institute of Acoustics, School of Physics Science and Engineering, Tongji University, 200092 Shanghai, China*

[4] *Institute of Structural Mechanics, Bauhaus-Universität Weimar, Weimar, D-99423, Germany*

[5] *Institut d'Electronique, de Microélectonique et de Nanotechnologie, UMR CNRS 8520, Département de Physique, Université de Lille, 59650 Villeneuve d'Ascq, France*

[6] *Institute of Photonics, Department of Mathematics and Physics, Leibniz University Hannover, Germany*

(Received 7 January 2022; revised 5 April 2022; accepted 3 June 2022; published 27 July 2022)

We present a non-Hermitian metabeam exhibiting an exceptional point (EP) induced by enforcing parity-time (*PT*) symmetry through applied external forces. The EP is formed by the hybridization of two flexural wave modes and its output displacement is enhanced by attaching two pillars on top of the beam. The introduction of a tiny mass perturbation that breaks the *PT* symmetry leads to a splitting of the eigenfrequencies at the EP with a square-root dependence on the perturbation mass. This effect manifests itself in a splitting of resonant peaks in the frequency response. The enhanced sensitivity of the EP paves the way to the detection of small perturbations such as tiny masses and cracks. Another property of the metabeam is the existence of skin modes whose energies are localized at one end of the beam and can be generated by implementing nonreciprocal feedback interactions between the pillars. We demonstrate that the skin modes are broadband and independent of the excitation positions. From a practical perspective, we show the great potential of skin modes in broadband energy harvesting. Our study proposes approaches to manipulate the non-Hermitian elastic wave phenomena, paving the way for the development of highly sensitive sensors, vibration control, and energy harvesting.

DOI: 10.1103/PhysRevApplied.18.014067

I. INTRODUCTION

The Hermiticity of a Hamiltonian depicts the conservation of energy in a closed system and shapes our understanding of physical reality. In many situations, however, the systems are not more conservative because of their interactions with the environment that result in gain or loss; these are known as non-Hermitian systems [1–4]. As such, their eigenfrequencies are generally complex, allowing for an increase or decrease in the system energy. In this context, lots of studies focus on a special kind of non-Hermitian system that preserves parity-time (*PT*) symmetry formed by balanced gain and loss [5,6]. The *PT* system was studied by Bender and Boettcher in 1998, demonstrating that *PT*-symmetric non-Hermitian Hamiltonians may exhibit purely real spectra [7,8]. There exists one transition point in the *PT* system, known as an exceptional point (EP), that defines a phase change from purely real to complex conjugate spectra. The EP is a spectral singularity in the parameter space exhibiting the simultaneous coalescence of two or more eigenvalues and their corresponding eigenvectors [2,9]. The EP exhibits different forms in different structures. In a finite structure, it is the degenerate point of two or more eigenfrequencies and corresponding eigenmodes of the structure [10,11]. In a waveguide structure, it is the degenerate point of the eigenvalues and corresponding eigenvectors of the scattering matrix [12,13]. EPs have received considerable widespread attention due to associated intriguing properties and exotic phenomena, such as unidirectional invisibility [14–17], laser mode selectivity [18,19], and enhanced sensitivity [11,20–23].

Outside of the scope of *PT* symmetry, an intriguing phenomenon is reported, known as the non-Hermitian skin effect, where a large number of the bulk modes of a one-dimensional (1D) system become localized toward the open boundaries [24–26]. Their existence crucially relies on nonreciprocal pumping or coupling between the adjacent sites [27,28]. By marrying non-Hermitian ingredients with nonreciprocal media, an unconventional non-Bloch bulk-boundary correspondence leads to unusual

*083623jinyabin@tongji.edu.cn
†zhuang@hot.uni-hannover.de

localization of bulk states at open boundaries [29,30]. The non-Hermitian skin effect manifests itself as extreme sensitivity to boundary conditions, namely that the eigenspectrum of the open boundary conditions dramatically differs from that calculated using periodic boundary conditions, which profoundly modifies the band topology and the bulk-boundary correspondence [31,32]. In the non-Hermitian skin effect, any injected signal, independent of its excitation position, always propagates in one direction, while the propagation in the opposite direction is strongly suppressed [25,33]. Recently, Zhang *et al*. experimentally demonstrated the higher-order non-Hermitian skin effect in a two-dimensional acoustic higher-order topological insulator, revealing the intriguing interplay between higher-order topology and non-Hermiticity [24]. For mechanical systems, Braghini *et al.* investigated nonreciprocal bands and skin modes in non-Hermitian elastic waveguides with piezoelectric feedback actuation [33]. Rosa, Mazzotti and Ruzzene investigated the skin modes of non-Hermitian 1D and 2D elastic lattices with nonlocal feedback control interactions [26]. These works that illustrate a variety of properties associated with non-Hermitian physics may pave the way to the design of non-Hermitian metamaterials with multiple functionalities. However, compared with optic and acoustic systems, the study of non-Hermitian EPs and skin modes for elastic wave systems is still at an early stage, and much more work is needed to investigate their construction mechanisms, underlying physical phenomena, and practical applicability.

The practical realization of gain and loss in *PT* systems has always been a difficult problem. The most commonly used method relies on the utilization of piezoelectric materials [13,34,35]. In most practical systems, given that gain is more challenging to achieve than loss, passive non-Hermitian systems without gain have been proposed, which can exhibit similar physical phenomena such as extreme asymmetric absorption [36,37]. On the other hand, the use of feedback interactions has been a common strategy in the study of skin modes [26,28,33]. Few methods of constructing EPs and skin modes in elastic wave systems have been proposed, however, as they are complicated to implement and they do not allow the EP and skin mode to be achieved in the same structure.

In this work, we propose a metabeam, constituted by a beam supporting pillars, where *PT* symmetry, and hence EPs, are achieved by the application of external forces with feedback. We demonstrate the frequency splitting of EPs both in eigenfrequencies and their responses under the effect of a tiny perturbation mass, which could be used as a detection method. Moreover, we realize the skin modes with their energy localized at one end of the same metabeam by changing the way of applying the external forces. We further demonstrate the great potential of skin modes for broadband energy harvesting. In this manner, the proposed metabeam has the merit of versatile operation and efficient tunability. Our results present a design of a non-Hermitian 1D elastic wave system, which may further enrich manipulation techniques for elastic waves based on phononic crystals and metamaterials [38,39].

This paper is organized as follows: In Sec. II, we present the design of the metabeam consisting of two pillars on a beam with *PT*-symmetric pairs of external forces. We demonstrate the existence of an EP formed by two flexural modes under specific external forces. We further numerically investigate the enhanced sensitivity of the EP to a tiny perturbation mass, which could be used as a nondestructive testing method. In Sec. III, we discuss the existence of skin modes in the metabeam by constructing nonreciprocal feedback interactions between the two pillars. We also demonstrate that most of their energy is localized at one end, independently of the excitation position, and show the great advantage of skin modes in broadband energy harvesting. Finally, we give a conclusion and briefly outline future research directions in Sec. IV.

II. EXCEPTIONAL POINT IN PT-SYMMETRIC METABEAM

A. *PT* symmetry proof of concept

Inspired by the pillared metaplate [40,41], the considered metabeam in this work, shown in Fig. 1(a), consists of two pillars connected to a thin aluminum beam by thin necks. The length, width, and thickness of the aluminum beam [$\rho = 2730$ kg/m^3, $E = 77.6$ GPa, $\nu = 0.352$ (Density ρ, Young's modulus E, and Poisson's ratio ν)] are 200, 10, and 1 mm. The two cylindrical necks are made of plastic ($\rho = 1190$ kg/m^3, $E = 3.2$ GPa, $\nu = 0.35$) with a height of 1.5 mm and a radius of 2 mm. The two pillars are made of tungsten alloy ($\rho = 19\,260$ kg/m^3, $E = 334.6$ GPa, $\nu = 0.28$) with a height of 44 mm and a radius of 4 mm. The positions of these components are labeled in Fig. 1(a). Equivalent non-Hermitian gain and loss mechanisms for the realization of *PT* symmetry and EPs can be established via applying external forces with feedback, as shown in Fig. 1(a). Here, the four external vertical forces are defined as

$$\begin{cases} N_1 = \gamma(\dot{w}_{2b} - \dot{w}_{1b}) \\ N_2 = -\gamma(\dot{w}_{2b} - \dot{w}_{1b}) \\ N_3 = -\gamma(\dot{w}_{4b} - \dot{w}_{3b}) \\ N_4 = \gamma(\dot{w}_{4b} - \dot{w}_{3b}) \end{cases} \tag{1}$$

where γ is the parameter defining the strength of gain and loss, $\dot{w}$ is the z component of the velocity and the subscripts of $\dot{w}$ represent the positions of the detected velocities depicted in Fig. 1(b). This metabeam is endowed with *PT* symmetry, in which the equivalent gain (loss) is conceptually introduced through the pair of forces N_1 and N_2 (N_3 and N_4). In other words, our metabeam has asymmetric gain and loss, with gain on the left half and

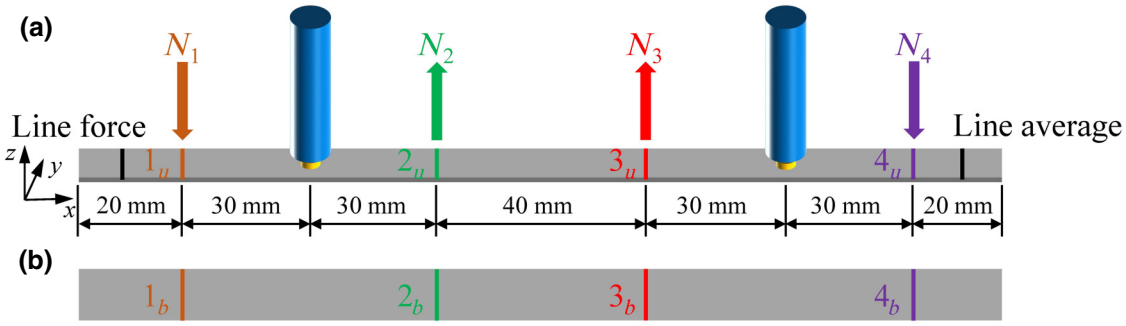

FIG. 1. (a) A metabeam possesses *PT* symmetry by applying external vertical forces with feedback. The pair of N_1 and N_2 (N_3 and N_4) forces can be regarded as equivalent to a gain (loss), which results in complex eigenfrequencies with negative (positive) imaginary parts. A vertical line force (black) at the left represents the source to excite flexural waves; the vertical displacement at the right of the beam is detected by a line detector (black). The beam, pillar's neck, and head are represented in gray, yellow, and blue, respectively. (b) The bottom surface of the metabeam, where four lines are used to detect the vertical velocities.

loss on the right half. In Appendix A, we describe in detail the effect of different pairs of forces on the imaginary parts of the eigenfrequencies of a bare beam and compare the trends with those obtained with material gain and loss, proving the feasibility of our scheme to achieve *PT* symmetry. From a practical point of view, the applied external forces can be achieved with piezoelectric elements. More specifically, the voltage applied to the transducers, and hence the forces they exert on the beam, are defined from the detection of the velocities at the positions 1_b to 4_b and the corresponding feedback to the controllers [11]. In the Supplemental Material [42], we use piezoelectric patches instead of forces to construct a metabeam with an EP (see Sec. IV of the Supplemental Material [42] for piezoelectric model details), which provides support for future experimental verification.

Now we focus on the existence of the EP of the proposed metabeam. First, we calculate the eigenspectrum of the metabeam in the Hermitian regime ($\gamma = 0$), as shown in Fig. 2(a). The original modes that coalesce under the non-Hermitian effect to form EPs are marked as blue points. Then, we calculate the eigenfrequencies of the metabeam as a function of γ and show the real and imaginary parts in Figs. 2(b) and 2(c), respectively. Here we define a polarization factor p to describe the degree of flexural polarization

$$p = \frac{\int |w|^2 dV}{\int (|u|^2 + |v|^2 + |w|^2) dV}. \tag{2}$$

u and v are x and y components of the displacement, respectively. The polarization factor p is employed to color code the scatter plots in Figs. 2(b) and 2(c), where red dots for $p \to 1$ identify predominantly flexural modes. There are two EPs in our metabeam in Fig. 2(b), which are highlighted by two green shaded zones. The four split branches in Fig. 2(c) indicate the bifurcation characteristics after the EPs. The original eigenfrequencies ($\gamma = 0$) of flexural

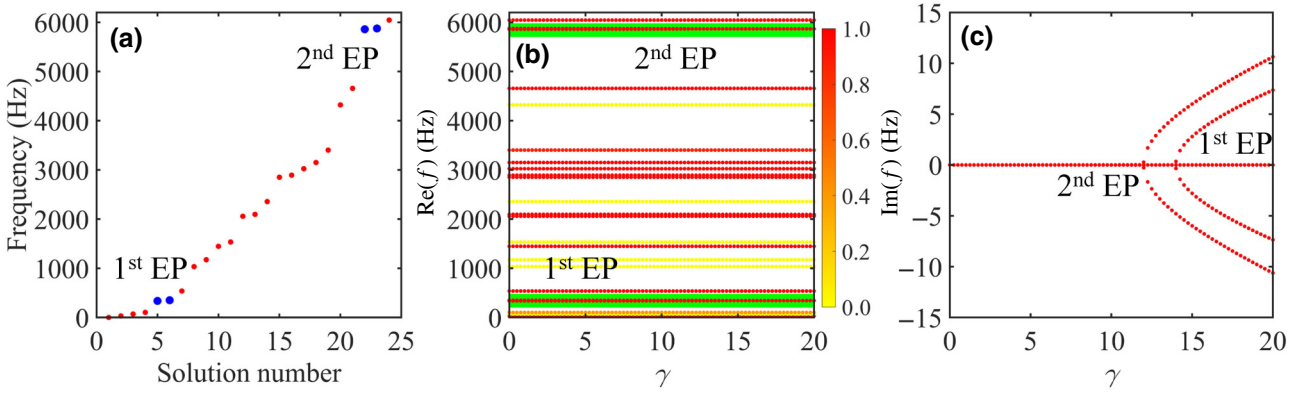

FIG. 2. (a) Calculated eigenspectrum for the system in the Hermitian regime ($\gamma = 0$) where γ defines the strength of the gain and loss [Eq. (1)]. Blue points indicate the original eigenfrequencies that could coalesce to form EPs. (b), (c) The variation of the real and imaginary parts of the eigenfrequencies of the system as a function of γ, respectively. The two green shaded areas highlight the positions of two EPs in our metabeam. The color scale represents the polarization factor p.

wave modes that could coalesce to form EPs are 336.0 and 350.4 Hz, and 5858.3 and 5874.2 Hz, respectively. It is important to know that the EPs are formed by the degeneration of two flexural wave modes with very close original eigenfrequencies under the non-Hermitian effect in our metabeam. EPs can also exist in other types of structures as long as the condition is met that the two original mode eigenfrequencies are close. We also show another kind of metabeam with a larger spring constant (the radius of the necks is changed from 2 mm to 2.5 mm, see the Supplemental Material [42] Sec. II for the other metabeam with EPs) that has three EPs in the studied frequency range.

Since the physical mechanisms and effects of EPs are the same, here we focus on a relatively high-frequency EP whose corresponding flexural wavelength is adapted to illustrate the study of its characteristics in our designed structure. We also show another EP whose frequency is relatively lower in the in the Supplemental Material [42] Sec. I. In Fig. 3(a), the original frequencies that could coalesce to form EPs in the non-Hermitian case are marked as blue points A and B at the frequencies of 5858.3 and 5874.2 Hz. These two modes, which are respectively symmetrical and antisymmetrical with respect to the middle position of the beam, display a high localization towards the two ends of the beam as shown in Figs. 3(c) and 3(d). However, their frequencies are relatively far from the compressional resonance of the individual pillars situated at 14 178 Hz. Figures 3(a) and 3(b) show the variation of the real and imaginary parts of the eigenfrequencies originating from points A and B when we gradually increase γ. The results obtained from the finite-element method (FEM) are expressed as hollow blue circles. For comparison and as a qualitative physical explanation, the system can be seen as a two-level system described by the coupled-mode theory (CMT) [43,44],

$$\frac{da_1}{dt} = i\omega_1 a_1 - \delta_1 a_1 + i\kappa_{12} a_2, \tag{3}$$

$$\frac{da_2}{dt} = i\omega_2 a_2 - \delta_2 a_2 + i\kappa_{21} a_1. \tag{4}$$

Here, a_1 and a_2 denote the complex displacement fields at the two free ends of the beam localized outside the two pillars, as shown in colorful regions in Figs. 3(c) and 3(d), where ω_1 and ω_2 represent each end's natural resonance frequency, κ_{12} and κ_{21} are the coupling strengths between them, and δ_1 and δ_2 are the gain and loss coefficients, respectively. Note that the left sides of Eqs. (3) and (4) actually represent velocities, which also explains the reason for using velocities in the expressions of the applied external forces in Eq. (1). To achieve the PT symmetry with balanced gain and loss, we can set $\omega_1 = \omega_2 \equiv \omega_0$, $\kappa_{12} = \kappa_{21} \equiv \kappa$, and $\delta_1 = -\delta_2 = \delta$. It is worth noting that δ has a different dimension from the γ we use in the metabeam, and the relation between γ and δ can be determined by fitting the position of the EP in the parameter space [44]. We can translate the coupled mode Eqs. (3) and (4) to a Schrödinger-type differential equation [45],

$$-i\partial_t|\psi\rangle = \mathbf{H}|\psi\rangle, \tag{5}$$

where $|\psi\rangle$ represents the states of the system, that is $|\psi\rangle = [a_1, a_2]^T$. $\mathbf{H}$ is the Hamiltonian and can be expressed as

$$\mathbf{H} = \begin{bmatrix} \omega_0 + i\delta & \kappa \\ \kappa & \omega_0 - i\delta \end{bmatrix}. \tag{6}$$

Then, by solving the eigenvalues of the Hamiltonian (6), the eigenfrequencies of the system are given by

$$\omega_\pm = \omega_0 \pm \sqrt{\kappa^2 - \delta^2}. \tag{7}$$

To determine the parameters, we first start with the Hermitian case, namely $\delta = 0$. In this case, Eq. (7) can be degenerated to $\omega_\pm = \omega_0 \pm \kappa$. With the initial values retrieved from the simulation in the Hermitian case, we can determine $\omega_0 = 5866.1$ and $\kappa = 8.0$ Hz. When gain and loss are introduced, the value of δ for each value of γ can be obtained from the splitting of the two modes. The CMT analytical results are plotted in Figs. 3(a) and 3(b) with red dots, and they are in good agreement with FEM results, the remarkable point being that the initial values of ω_0 and κ remain fixed and do not need to be adjusted from their original values when we change γ.

From Fig. 3, we can clearly see the evolution of the eigenfrequencies of the PT system and the emergence of the EP when we gradually increase γ. The real parts of eigenfrequencies gradually approach each other and then merge to form the EP at $\gamma = 12$, while the imaginary parts bifurcate into two branches beyond the EP. It is worth mentioning that our metabeam is a finite resonant structure, so the EP is generated by the coalescence of the eigenfrequencies and eigenmodes of the finite structure. In our system, the EP is formed by two original eigenfrequencies and is called a second-order exceptional point [20]. The total displacement fields corresponding to the five eigenmodes marked A–E in Figs. 3(a) and 3(b) are shown in Figs. 3(c)–3(g). It is evident that, before the EP, the eigenmodes still preserve the displacements at the two ends. In this regime, also known as the PT-exact phase regime, the energies of the eigenmodes are distributed at the two ends of the beam. It is worth noting that the displacement fields localized in the left and right ends in modes A and B are antisymmetric and symmetric, respectively. Thus, at the EP mode C, obtained from the coalescence of modes A and B, the displacement field at the right end of the beam is preserved while the field at the left end vanishes, as depicted in Fig. 3(e). We also show the modes D and E (with eigenfrequencies $5866.1 - 5.98i$ and $5866.1 +$

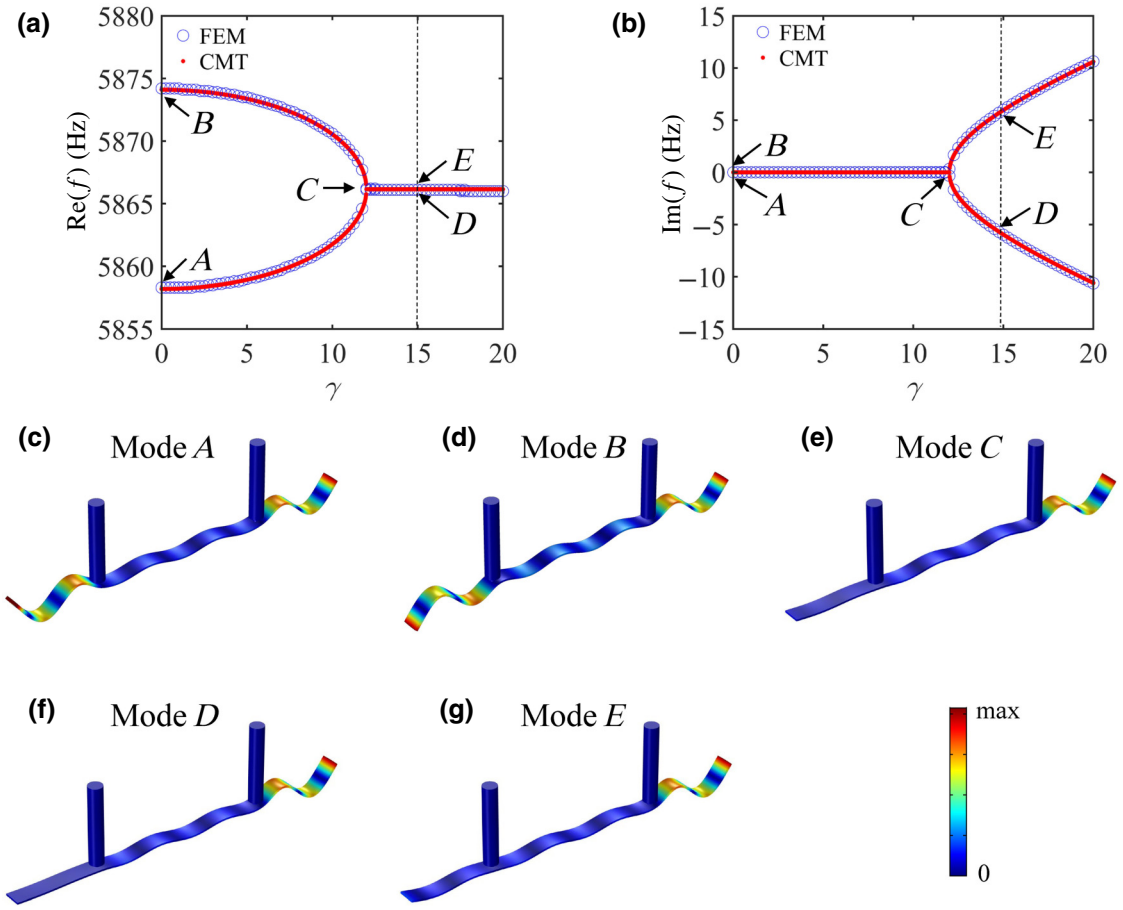

FIG. 3. (a), (b) The variation of the real and imaginary parts of the eigenfrequencies originating from points A and B as a function of γ, respectively. The hollow blue circles and red dots represent the FEM and CMT results, respectively. (c)–(g) The mode shapes of the points marked in (a) and (b). The color scale represents the magnitude of total displacements.

5.98i Hz, respectively) at $\gamma = 15$ in the PT-broken phase regime in Figs. 3(f) and 3(g), whose displacement fields are close to that at the EP. Note that the lowest resonant frequency of the pillars is at about 14 178 Hz so the features shown in Figs. 3(c)–3(g) around the EP frequency do not have a direct relationship with the pillar's resonance. The calculated eigenfrequencies are those of the whole system including the beam and the pillars. In addition, the γ value corresponding to the EP varies for different distances between the two forces in a pair. An illustration of the influence of the distance between the applied forces on the EP is given in Appendix B. It is worth noting that the EP can also be achieved by applying appropriate feedback forces on a beam without any pillars, like in reference [11]. However, in this reference, the EPs were formed from the hybridization of a longitudinal ($S0$) and a flexural ($A0$) mode, while in our design the EP results from the coalescence of two flexural waves, so it also corresponds to flexural motion. Additionally, the original modes A and B whose displacements are localized at both ends of the beam are the prerequisites for achieving the skin modes in the metabeam in Sec. III, which are impossible to achieve in a bare beam. Another important point to note is that our geometrical parameters are chosen in such a way as to bring the frequencies of the two initial flexural modes close to each other, which is a requirement to achieve their coalescence after exerting the external forces. In addition, we discuss the influence of the pillars' height (thus their resonant frequency) on the metabeam. The results show that the pillar parameters slightly affect the EP frequencies and CMT parameters but do not change the physical discussions and trends (see the Supplemental Material [42] Sec. III for the detailed results).

To further investigate the physical meaning of the PT system, we calculate the frequency responses of the flexural waves propagating in the metabeam under different γ values. We apply a vertical line force (which is taken to be equal to 10 N/m, unless stated otherwise) to the left of N_1 and receive the vertical displacements at the line on the right of N_4, as shown in Fig. 1(a). We show in Fig. 4, the vertical response displacements $|w|$. In the Hermitian case [Fig. 4(a)], the frequency response has two peaks

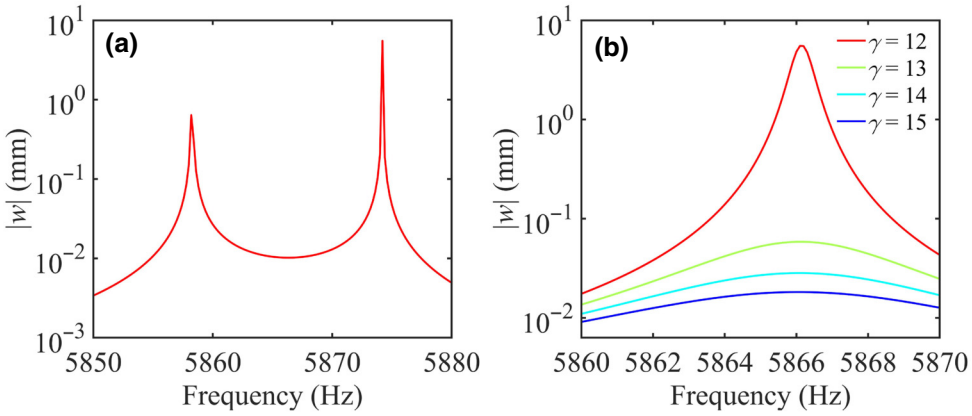

FIG. 4. The frequency responses of the flexural waves propagating in the metabeam when (a) $\gamma = 0$ and (b) $\gamma =$ 12, 13, 14, and 15.

corresponding to resonant frequencies A and B in Fig. 3(a). However, at the EP ($\gamma = 12$), only one peak exists due to the coalescence of the two eigenfrequencies, as shown by the red curve in Fig. 4(b). We also notice that the response displacement is greatly enhanced at the frequency 5866.1 Hz of the EP. Note that at this peak corresponding to the EP ($\gamma = 12$), the applied vertical forces N_1 and N_2 should be equal to 2.76×10^3 N/m, whereas the forces N_3 and N_4 become 1.41×10^3 N/m. On the other hand, we observe that in Fig. 4(b) the response peaks gradually vanish and the curves become smooth with increasing values of γ. This is because beyond the EP, the imaginary parts of the eigenfrequency increase with γ, resulting in greater attenuation in frequency responses.

B. Enhanced sensitivity at the exceptional point

Now we focus on the EP shown above. The EP has many peculiar properties, of which the most commonly used is the enhanced sensitivity to small perturbations [2,11,20,22]. Here we show the high sensitivity of the EP in our proposed metabeam to the addition of a small mass at the center of the top surface of the beam.

The perturbation mass is placed at the center of the top surface of the aluminum beam, as depicted in Fig. 5(a). First, we start with a 20-mg mass and study the response of the EP. It should be emphasized that a 20-mg mass is about 0.02% of the total mass of the system, which is equal to 96.2 g. Under this circumstance, the real parts of eigenfrequencies of the metabeam drastically change, and the EP moves to a higher γ value, as shown in Fig. 5(b). If we choose $\gamma = 12$ as the baseline (green dashed line), the frequency splitting occurs under the added mass perturbation. To prove this, we calculate the frequency responses in these two cases at $\gamma = 12$, and the results are plotted in Fig. 5(c). This clearly illustrates that the initial single response peak (blue line) splits into two separate peaks (red line) in the presence of the additional mass. The frequency splitting is about 8 Hz for a mass of 20 mg, which is enough to be measured in practice.

Next, we characterize the bifurcation behavior of the second-order EP associated with this PT system. We calculate the frequency responses of our metabeam at $\gamma = 12$ when changing the value of the perturbation mass and normalize the displacements according to the maximum value of each case. The results are shown in Fig. 6(a), in which the bright positions represent the response peaks. One can note an increase in the splitting of the two modes when increasing the perturbation mass. This splitting depicted in Fig. 6(b) displays a square-root-like behavior. This is confirmed by the linear slope of 0.535 in the corresponding logarithmic plot shown in the inset of Fig. 6(b). The slight deviation from a slope of 0.5 may be caused by the fitting methods and simulation accuracy. Figure 6(c) depicts the sensitivity defined as $\Delta\omega/\epsilon$ as a function of the perturbation mass. The decrease in the sensitivity is close to a $\Delta\omega/\epsilon \propto \left(1/\sqrt{\epsilon}\right)$ behavior as can be seen in the logarithmic presentation in the inset with a slope of -0.465. The sensitivity increases as the perturbation mass ϵ decreases due to the presence of the second-order EP. The unique nature of the EP provides us with a way to detect a tiny mass. When there is a perturbation mass, we can obtain the frequency splitting value by measuring the response peak frequencies of the system at the undisturbed EP, then predict the mass according to the frequency splitting in Fig. 6(b). Additionally, the displacements at resonant frequencies are greatly enhanced by the metabeam resonances and are easier to measure in the experiment. Note that the frequency splitting in the vicinity of the EP can be applied to other small perturbations; for example, the presence of small cracks or structural defects will also have similar effects on the EP.

Furthermore, we investigate the responses of the EP if the position of the perturbation mass is moved from the center. First, we place a 20-mg mass at the center and move it along the positive x direction. In this case, the

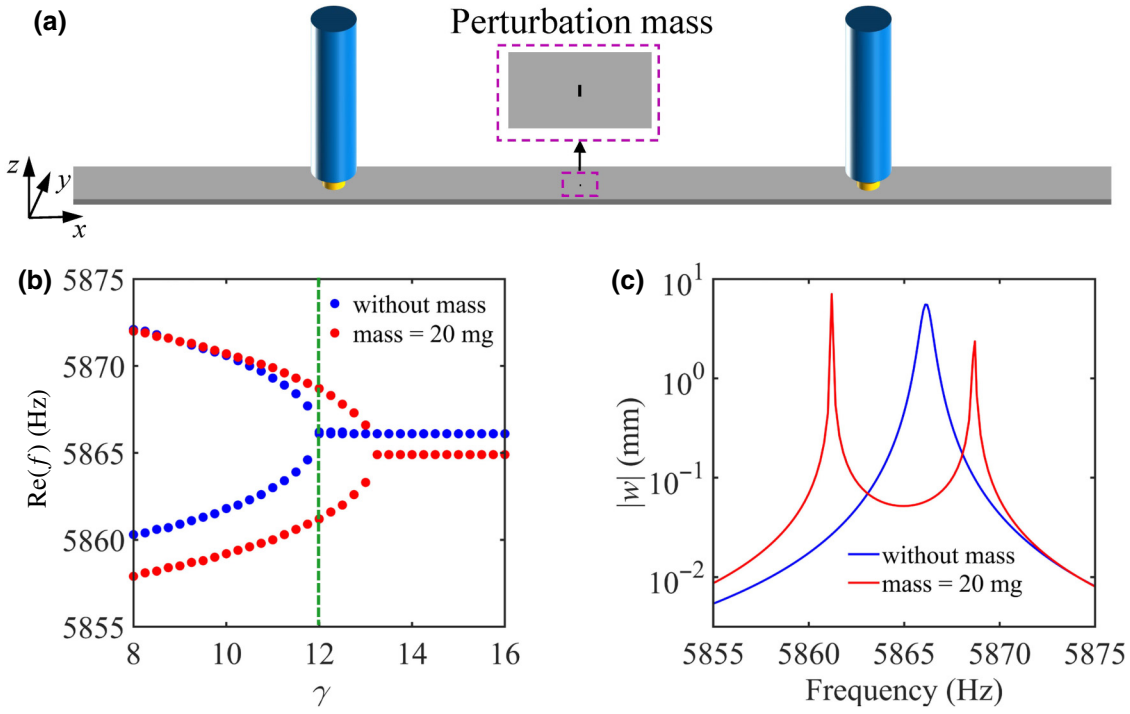

FIG. 5. (a) The illustration of a perturbation mass placed at the center of the top surface of the metabeam. The magenta dashed box gives an enlarged view of the perturbation mass. (b) The variation of the real parts of the eigenfrequencies of the metabeam without perturbation mass (blue dots) and with 20-mg mass (red dots) with varying γ. The EP changes its position under the influence of the tiny perturbation mass. (c) The frequency responses in the two cases at $\gamma = 12$ [green dashed line in (b)].

amplitudes of the response peaks decrease and the whole curve becomes smooth even for a deviation of 1 mm [light green line in Fig. 7(a)]. If the mass is moved further, this trend becomes more apparent, and the peaks almost disappear at a deviation of 3 mm [blue line in Fig. 7(a)]. This behavior is due to the deviation from the *PT* symmetry that produces an increase in the imaginary parts of the resonance frequencies, resulting in higher attenuation and a smoother response curve. When the mass is not offset, the two eigenfrequencies of the metabeam are 5861.2 and 5868.7 Hz. By moving the mass by 1, 2, or 3 mm along the x direction, the eigenfrequencies become $5861.2 - 0.97i$ and $5868.6 + 0.92i$ Hz, $5861.3 - 1.89i$ and $5868.5 + 1.80i$ Hz,

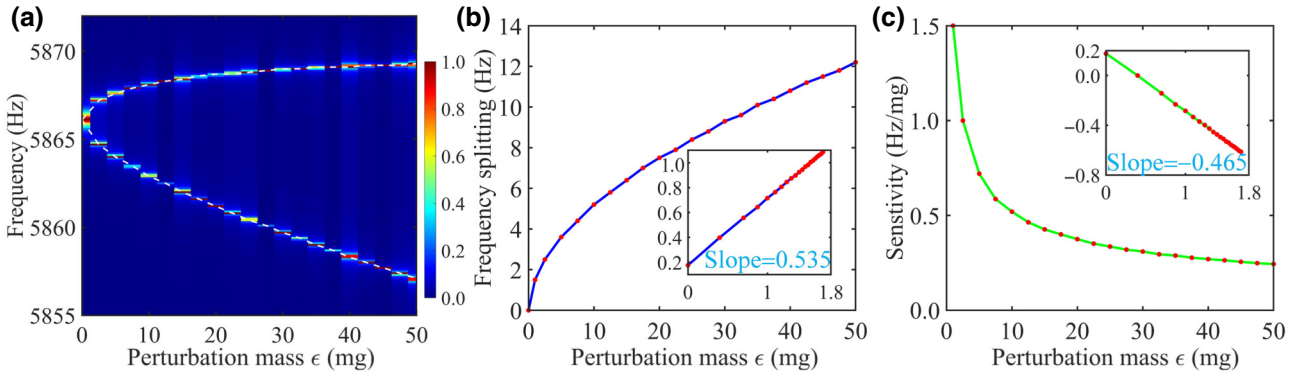

FIG. 6. (a) The normalized response displacement spectra of the metabeam under different perturbation masses. The color scale represents the normalized vertical displacements at the detection line. The white dashed line connects response peaks at different perturbation masses to clearly show the bifurcation behavior. (b) Resonant frequency splitting as a function of the perturbation mass ϵ, in which the red dots are data points connected by the blue line as a guide to the eyes. The inset demonstrates a slope of 0.535 on a logarithmic scale, confirming the relationship $\Delta\omega \propto \sqrt{\epsilon}$ for a second-order EP. (c) Sensitivity as a function of the perturbation mass ϵ, in which the red dots are data points connected by the green line. The inset shows a slope of -0.465 on a logarithmic scale, confirming the relationship $\Delta\omega/\epsilon \propto \left(1/\sqrt{\epsilon}\right)$ for a second-order EP. All these results are calculated at $\gamma = 12$.

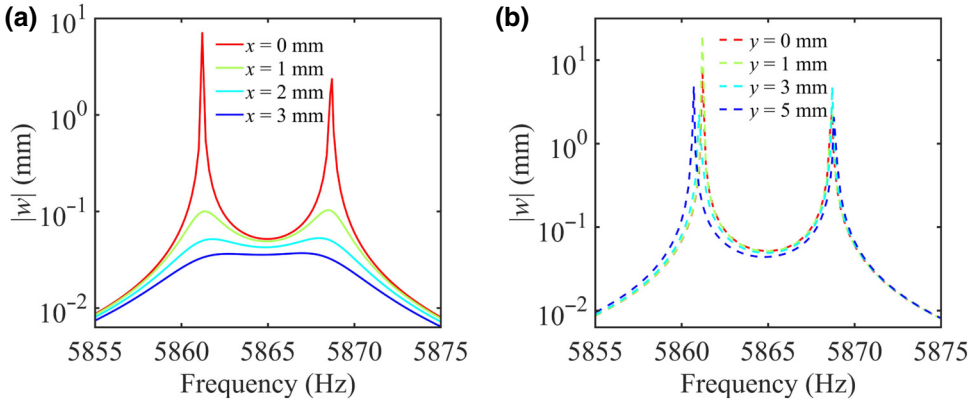

FIG. 7. The frequency responses of the metabeam when the location of a 20-mg mass deviates from the center and breaks the *PT* symmetry. (a), (b) The results when the mass moves along the positive x direction and y direction, respectively. All these results are calculated at $\gamma = 12$.

and $5861.3 - 2.73i$ and $5868.2 + 2.61i$ Hz, respectively. The physical mechanism of this phenomenon is the same as in Fig. 4(b), namely an increase in the imaginary parts of the eigenvalues. Similar results are obtained if we move the mass along the negative x direction. The trend is different if the mass is moved along positive or negative y direction [Fig. 7(b)]. In this case, the frequency splitting slightly increases but the response peaks and curves are not significantly affected. By moving the mass by 1, 3, or 5 mm along the y direction, the eigenfrequencies of the metabeam become 5861.2 and 5868.7 Hz, 5861.0 and 5868.7 Hz, 5860.7 and 5868.8 Hz, respectively. These results indicate that moving the mass along the y direction has a slight influence on the real parts of eigenfrequencies, while moving mass along the x direction mainly impacts the imaginary parts.

Let us note that due to the *PT* symmetry, the frequency response is reciprocal. Namely, the positions of the source and detector can be inverted and the same displacement field is obtained.

III. SKIN MODES IN THE METABEAM

In this section, we make another arrangement of the applied external forces on the metabeam and their feedback conditions to obtain the so-called skin modes that are localized at one end of the beam. To break down the response reciprocity and realize skin modes, we construct a feedback interaction between two pillars by applying external forces at both sides of one pillar, which are related to velocities of two lines at both sides of the other pillar, as illustrated in Fig. 8(a). The applied external forces N_5 and N_6 are defined as

$$\begin{cases} N_5 = \alpha(\dot{w}_{1u} - \dot{w}_{2u}) \\ N_6 = -\alpha(\dot{w}_{1u} - \dot{w}_{2u}) \end{cases}, \tag{8}$$

where α is an amplification coefficient, $\dot{w}$ is the z component of the velocity, and the subscripts of $\dot{w}$ represent the positions of detected velocities depicted in Fig. 8(a). The skin effect results from the interplay between non-Hermiticity and nonreciprocity. Nonreciprocity can be achieved by using passive structures combining broken spatial symmetries and nonlinearities [46], or using active time-modulated components that break time-reversal symmetry [47]. Here we use feedback control to break reciprocity at the level of the interactions between the pillars [28]. Specifically, the metabeam responds differently (i.e., different feedback forces) to waves propagating in positive and negative directions. It should be mentioned that the role of the feedback method used for skin modes is to construct nonreciprocal interactions between two pillars, in contrast to individual feedback mechanisms for each pillar in *PT* symmetry [28,33] studied in the previous section. We first arbitrarily choose $\alpha = 1000$, and show the eigenfrequencies of the metabeam in Fig. 8(b). The results with different α values are illustrated in Appendix C. The irregular trend of the imaginary parts of the eigenfrequencies in Fig. 8(b) can be understood by the fact that the applied forces are vertical, so they only affect the flexural modes of the metabeam while leaving other modes such as torsional modes unaffected and purely real. Another condition for achieving skin modes in our system is that the displacements of the original modes in the Hermitian regime need to be localized at both ends of the beam, such as in Figs. 3(c) and 3(d). Moreover, the imaginary parts of the skin modes should be small enough to avoid attenuation during metabeam response. Thus, we choose mode 1 and mode 2 [blue points in Fig. 8(b)] corresponding to mode A and mode B in Fig. 3 to demonstrate the skin mode. Now the eigenfrequencies of the metabeam have changed from the original values 5858.3 and 5874.2 Hz to $5890.8 - 2.51i$ and $5918.7 + 210.37i$ Hz. The corresponding mode shapes are shown in Figs. 8(c) and 8(d). We can

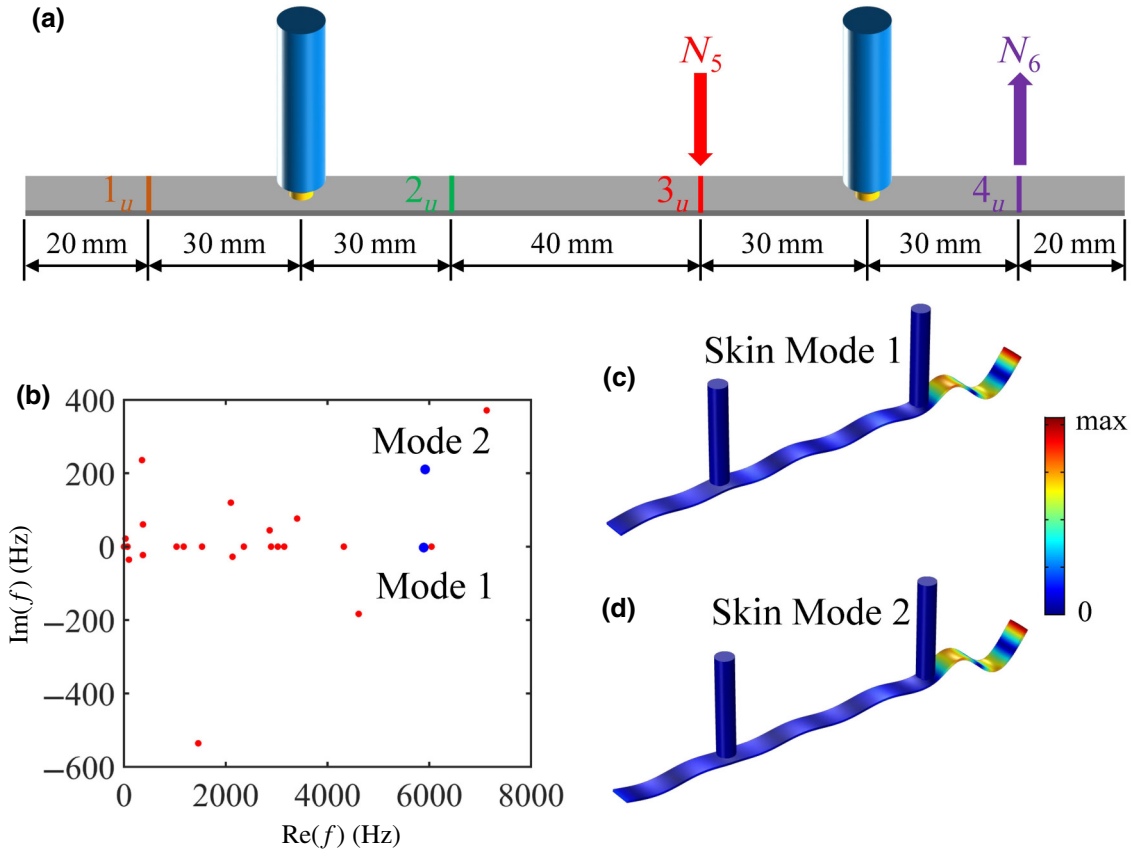

FIG. 8. (a) Illustration of a metabeam possessing non-Hermitian skin modes by applying nonreciprocal feedback interactions between the two pillars. (b) The eigenspectrum of the system when $\alpha = 1000$ [see Eq. (8)]. The two skin modes are marked as blue points. (c), (d) The displacement fields of the skin modes at the eigenfrequencies $5890.8 - 2.51i$ Hz and $5918.7 + 210.37i$ Hz, respectively. The color scale represents the magnitude of total displacements.

see that the total displacements of the two skin modes are concentrated on the right end, compared with the original modal displacements on both sides [Figs. 3(c) and 3(d)]. The two skin modes seem similar but their slight difference can be seen in the left end of the beam. It is worth noting that although the two skin modes and EP mode [Fig. 3(e)] have very similar localization, they have totally different physical meanings. We verify this in the frequency domain calculations discussed in the following. First, let us point out that the skin mode is often studied by band structure in periodic non-Hermitian structures [28,33]. However, the skin mode is ultimately achieved within finite structures with open boundaries. There is no essential difference between the skin mode constructed by our metabeam with open boundaries and the skin mode constructed by multiple periodic elements. On the other hand, we also use piezoelectric patches to construct a metabeam with a skin mode (see Sec. V of the Supplemental Material [42] for piezoelectric model details), which could support future experimental verification. Furthermore, we discuss the influences of global loss on metabeams with EPs and skin modes. The results show that the loss reduces the peak response displacements and makes the curves smooth (see Sec. VI of the Supplemental Material [42] for the loss effects).

The essential feature of a non-Hermitian skin mode is that most of the energy propagates in one direction and becomes localized at one end, while the propagation in the opposite direction is strongly suppressed [25]. Thus, we calculate the frequency responses of the flexural waves in the frequency domain when varying the excitation positions, and the results are illustrated in Fig. 9(a). The excitation line force used here is 100 N/m. The capital letters M, L, R used in the legend represent the excitation source located at the middle, left, and right, respectively. The subscripts r and l refer to the detected displacements at the right or the left, respectively. The six response curves show the same trends as a function of frequency. It can be seen that no matter where the excitation source is located, the response displacement on the right side (dashed lines) is always about 10 times larger than that on the left side (solid lines). Let us note that the two curves L_l and R_r overlap because both curves represent the displacement at the excitation source position. Figure 9(a) tells us that the

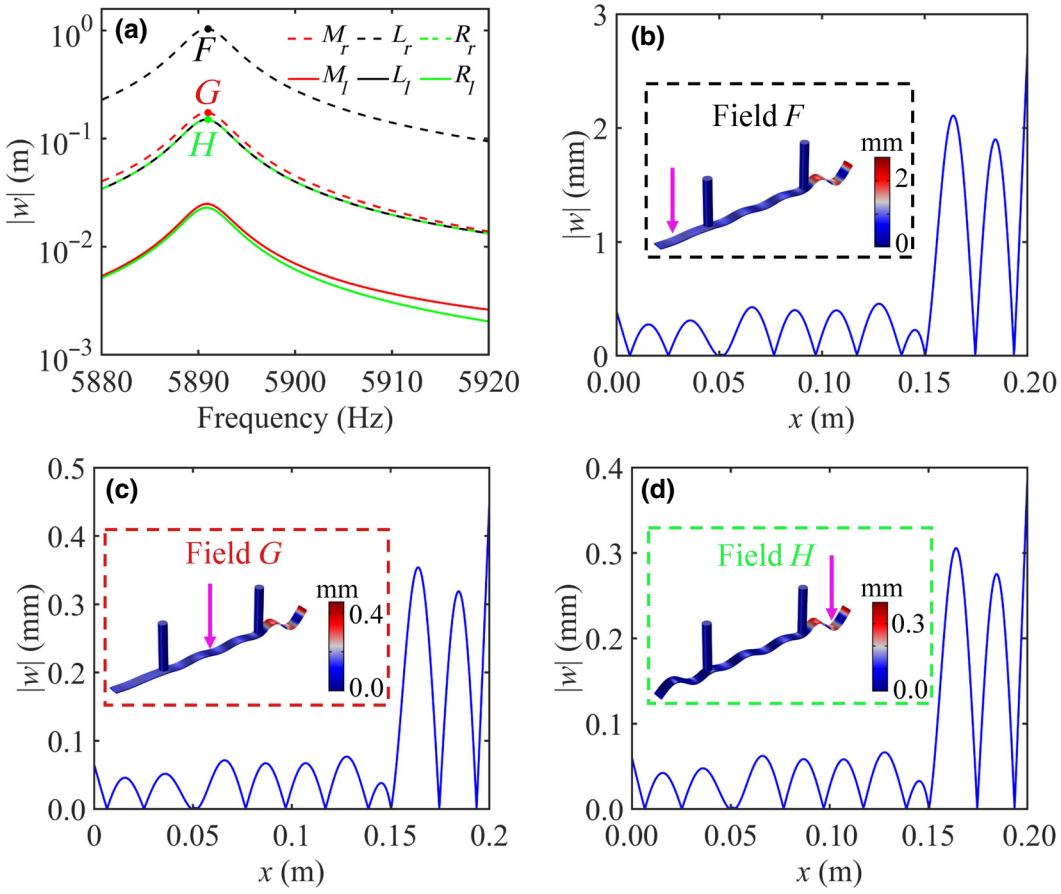

FIG. 9. (a) The frequency responses of the flexural waves propagating in the metabeam with the excitation source located at the left (L), middle (M), or right (R). The subscripts r and l associated with each curve refer to detection at the right or the left, respectively. Points F, G, and H representing the response peaks all appear at a frequency of 5891 Hz. (b)–(d) The vertical displacements along the beam corresponding to F, G, and H, respectively. The insets show the maps of the vertical displacement fields. The magenta arrows indicate the excitation positions, and the color scales represent the magnitude of $|w|$.

vertical displacements at the right end are always greater than the displacements at the left end, no matter the position of the force source. This is particularly striking in the case of middle excitation, where most energy tends to flow to the right rather than to the left. Moreover, the vertical displacements are maximum in the case of left excitation because the detected difference in velocities between positions 1_u and 2_u under the left excitation is the greatest, resulting in the largest feedback to the external forces N_5 and N_6. It is worth noting that the external forces are equal to 323 N/m at the response peak under the left excitation. In addition, only one response peak at 5891 Hz appears in all three cases (points F, G, and H), consistent with the resonance frequency $5890.8 - 2.51i$ Hz. However, there is no peak around the other resonant frequency $5918.7 + 210.37i$ Hz. Indeed, the imaginary part of the latter mode is much greater, resulting in higher attenuation.

Next, vertical displacements along the beam at the frequencies of points F, G, and H [Fig. 9(a)] are displayed in the main plots of Figs. 9(b)–9(d), respectively. The three curves have similar shapes, in that most of the displacements are located between 0.15 and 0.2 m, despite the different amplitudes. The insets in the three figures show the corresponding maps of the vertical displacement fields, in which the magenta arrows indicate the location of the excitation force, and the color scales represent the magnitude of $|w|$. One can clearly see that in all cases, most of the highest displacements are localized at the right end, which behaves as a trap for energy. Although we only list the fields at the peaks, the skin modes are broadband, although their amplitudes decrease when we depart from the peaks. Furthermore, if we want to make the displacements localized to the left, we just need to switch the positions of detected velocities and applied external forces. Now we can summarize that although the mode shapes of the EP mode and skin mode are similar in our work, there are essential differences between them: the EP is reciprocal and easily affected by external conditions, while the skin

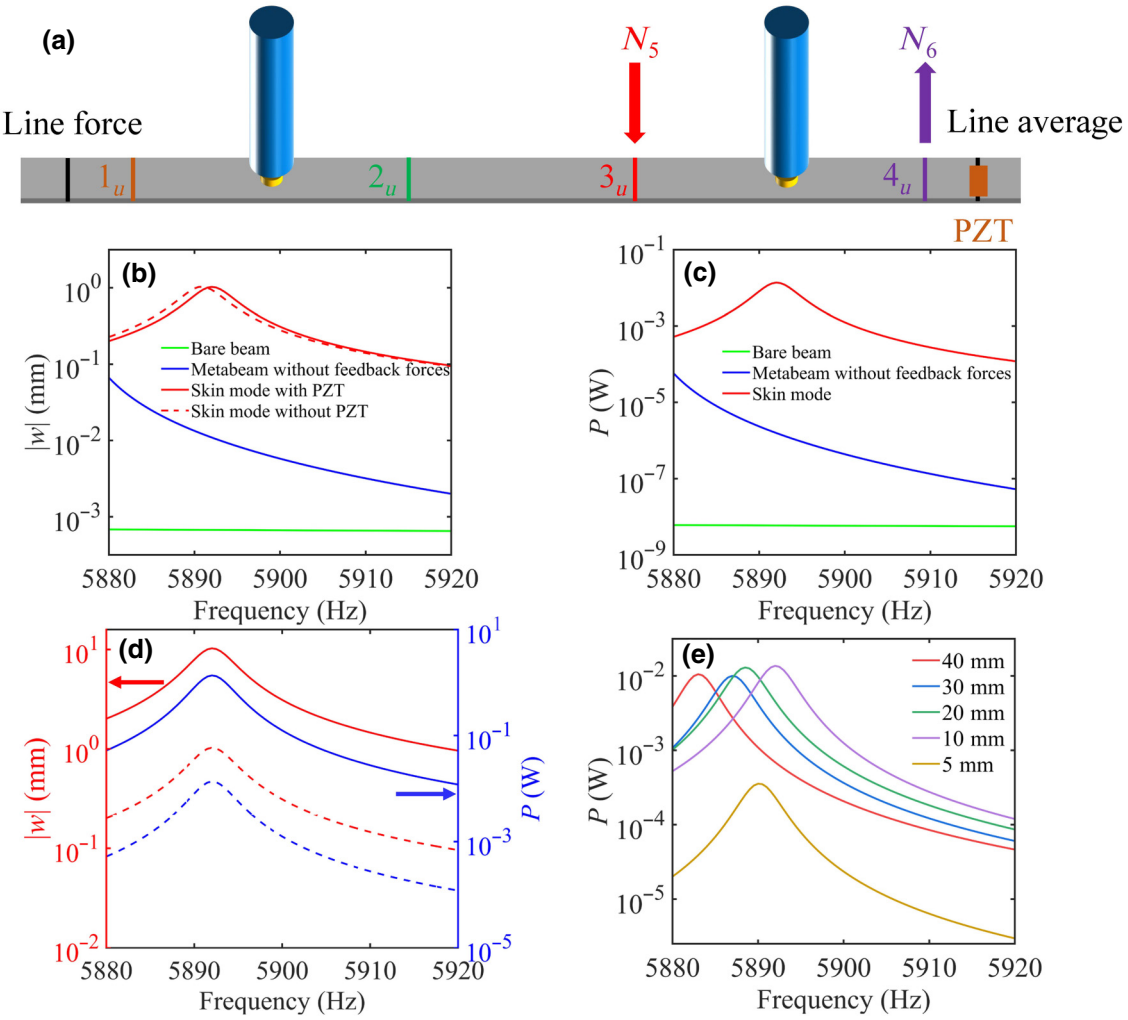

FIG. 10. (a) The illustration of energy harvesting by a PZT patch attached at the location of the skin mode under left excitation. (b) Right line vertical displacement average $|w|$ in different cases. (c) PZT output power P for the bare beam, metabeam without feedback forces, and with feedback forces giving rise to the skin mode. (d) The vertical displacements $|w|$ and output power P with an excitation force of 100 N/m (red and blue dashed lines, respectively) and 1000 N/m (red and blue solid lines, respectively). (e) The variation of output power P with different PZT locations where the legends denote the distances between the PZT center and the right boundary of the beam.

mode is nonreciprocal and immune with respect to the excitation location.

The skin modes have a great potential for highly efficient energy harvesting from a practical point of view. To highlight this capacity, we adopt a rectangular piezoelectric Lead Zirconate Titanate (PZT)-5H patch and attach it to the top surface of the beam at the line average as shown in Fig. 10(a). The length, width, and thickness of the PZT patch used here are 5, 1, and 0.2 mm, respectively. With the electromechanical coupling effect, the vibrating energy of the beam can be transformed into electric power. The vertical excitation line force applied at the left of the beam is 100 N/m and the amplification coefficient is chosen as $\alpha = 1000$. A simple circuit powered by the PZT patch with a resistance $R = 100\ \Omega$ is devised, with an output power P defined as [48,49]

$$P = \frac{VI}{2} = \frac{RI^2}{2}, \tag{9}$$

where V and I are the voltage and current across the resistance R, respectively.

We first compare in Fig. 10(b) the average detected line displacement $|w|$ for four situations: a bare beam without any feedback forces (green line), a metabeam without feedback forces (blue line), a metabeam with feedback forces (that give rise to the skin mode) with the attached PZT patch (red solid line), or without the PZT patch (red dashed line) cases. The displacements of the skin mode

within the calculated frequency range are much higher than those associated with the metabeam without feedback forces or with the bare beam. The red solid and dashed lines are basically identical, indicating that the PZT patch has almost no influence on the skin mode, except that the peak frequency is slightly increased. The output power P calculated by Eq. (9) is depicted in Fig. 10(c). This shows that the output power associated with the skin mode within the calculated frequency range is 1–4 orders of magnitude higher than that of the metabeam without feedback forces and 4–6 orders of magnitude higher than that of the bare beam. The output power has broadband stability due to the skin mode. In addition, we calculate the output power for the bare beam with the same external sources as skin modes (including the same sources of excitation, and external feedback forces N_5 and N_6) to compare the output power between two systems with or without metastructures. The results (see Sec. VII of the Supplemental Material [42] for the output power comparison) show the obvious advantage in the output power ratio of our metabeam. Additionally, the variation trends of $|w|$ and P under two excitation forces of 100 N/m (red and blue dashed lines, respectively) and 1000 N/m (red and blue solid lines, respectively) are calculated and plotted in Fig. 10(d). One can notice that the four curves have the same shape owing to the electromechanical coupling effect. When the excitation force is increased 10 times, the response displacement also increases 10 times, but the output power increases 100 times. We also study the influences of the PZT locations on output power, as shown in Fig. 10(e). On the one hand, the PZT output power becomes very small when the PZT is close to the free end as depicted by the yellow line. In the other four cases, the output power is in the same order of magnitude, but slightly larger at 10 and 20 mm (purple and green lines). On the other hand, the frequency corresponding to the output power peak decreases when the PZT moves toward the pillar. Thus, the PZT location may have a significant impact on the energy harvesting in the metabeam. Furthermore, although the localized displacements and output power for middle and right excitation are smaller than that for left excitation, they are still relatively considerable and they retain broadband stability. Thus, the skin mode with energy localization on one end is very suitable and practical for broadband energy harvesting.

IV. CONCLUSIONS

In conclusion, we propose metabeams with PT symmetry or non-Hermitian skin modes through the application of external forces with feedback. The EP is generated by two resonant flexural modes of the metabeam and has enhanced output displacements. We illustrate that the response of the second-order EP for small perturbations exhibits a square-root behavior, which could be used as a potential detection strategy for small perturbations such as a tiny mass. Furthermore, the EP responds differently and irregularly when the location of the perturbations deviates from the center of symmetry. This will be the object of forthcoming work. In addition, we achieve the skin mode of flexural waves by constructing nonreciprocal feedback interaction between two pillars, which could be used to extract mechanical energy, allowing energy to flow in one direction and preventing it from flowing in the other direction. We show the great potential of skin modes for broadband energy harvesting. The proposed strategy may open promising avenues for designing elastic wave devices for communication and sensing [50,51], energy harvesting [52–55], and vibration control [56,57]. Moreover, unlike other ways to achieve EPs or skin modes, the proposed strategy has some advantages, such as practical realization, easy measurement, and *in situ* tunability. Our results may pave the way towards a class of non-Hermitian elastic wave systems. Finally, several opportunities are identified for future studies, such as the design of higher-order EPs with higher sensitivity, time-space modulated metamaterials, or higher-order skin modes.

The data that support the findings of this study are available from the corresponding authors upon reasonable request.

ACKNOWLEDGMENTS

This work was supported by the National Natural Science Foundation of China (Grants No. 11902223 and No. 12074286), the Young Elite Scientists Sponsorship Program by CAST (2021QNRC001), the Shanghai Science and Technology Committee (Grant No. 21JC1405600), the program for professor of special appointment (Eastern Scholar) at Shanghai Institutions of Higher Learning, and the Fundamental Research Funds for the Central Universities.

APPENDIX A: IMPACT OF FEEDBACK FORCES ON THE EIGENFREQUENCIES OF A BARE BEAM

In order to illustrate the effect of applied forces on the structure, we take a bare aluminum beam as an example and investigate the change of its eigenfrequencies under two situations. In the first case, we change the material properties by assuming a loss or gain. In the second case, we apply external forces to the beam.

First, we impose opposite imaginary parts to the shear modulus of the beam [58], i.e., $G = G_0(1 \pm 0.01i)$, where $G_0 = 28.7$ GPa is the shear modulus of aluminum. The negative (positive) imaginary part of G represents material gain (material loss). The material loss has the consequence that the imaginary parts of the eigenfrequencies become positive and they increase as the frequency increases [see

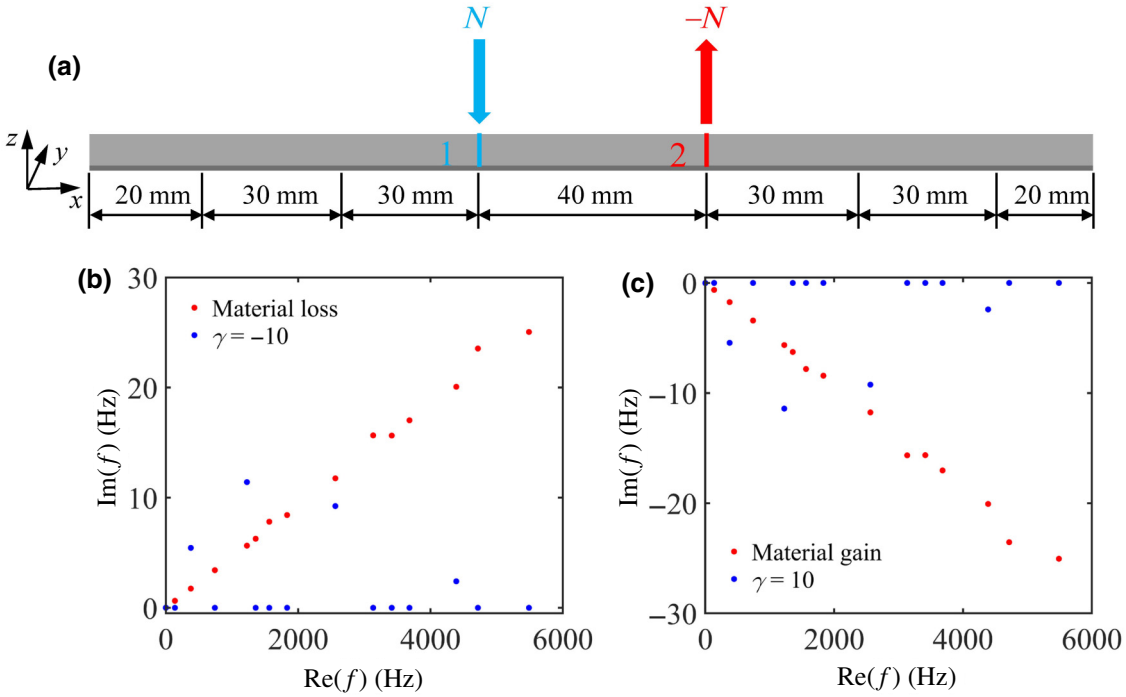

FIG. 11. (a) The illustration of external forces on a bare beam in which $N = \gamma(\dot{w}_1 - \dot{w}_2)$. (b) The variation of eigenfrequencies of the bare beam under material loss (red dots) or external forces with $\gamma = -10$ (blue dots). (c) The variation of eigenfrequencies of the bare beam under material gain (red dots) or external forces with $\gamma = 10$ (blue dots).

red dots in Fig. 11(b)]. This is consistent with the physical intuition that high-frequency waves are more easily affected by the material property. In contrast, the material gain gives rise to negative imaginary parts in the eigenfrequencies [red dots in Fig. 11(c)]. Their absolute values are equal to those of the positive imaginary parts in the case of material loss.

Now, we apply a pair of opposite forces related to the velocities as illustrated in Fig. 11(a). The left force is defined as $N = \gamma(\dot{w}_1 - \dot{w}_2)$, where $\dot{w}_1$ is the vertical velocity of line 1 and $\dot{w}_2$ is the vertical velocity of line 2 in Fig. 11(a), respectively. The right force is equal to the force on the left, but is applied in the opposite direction. Because the forces are applied perpendicular to the beam, only eigenfrequencies of flexural modes are affected and display positive imaginary parts when $\gamma = -10$, as shown by blue dots in Fig. 11(b). Note that there is no obvious trend between the imaginary and real parts of the eigenfrequencies since we apply forces instead of material loss. On the other hand, eigenfrequencies of flexural modes display negative imaginary parts when $\gamma = 10$ and their absolute values are equal to the positive imaginary parts in the case $\gamma = -10$, as shown by blue dots in Fig. 11(c). These results indicate that we can achieve the same effect on eigenfrequencies of the structure either by modifying material parameters (loss or gain) or by applying external forces. When γ is positive, the eigenfrequencies of the flexural modes have negative imaginary parts, which can be regarded as equivalent to a gain (the pair of N_1 and N_2 in Fig. 1); when γ is negative, the eigenfrequencies of the flexural modes have positive imaginary parts, which can be regarded as equivalent to a loss (the pair of N_3 and N_4 in Fig. 1).

APPENDIX B: INFLUENCE OF DISTANCE BETWEEN THE APPLIED FORCES ON THE EP

We calculate the γ value of the EP at different distances between the applied forces in a pair and summarize

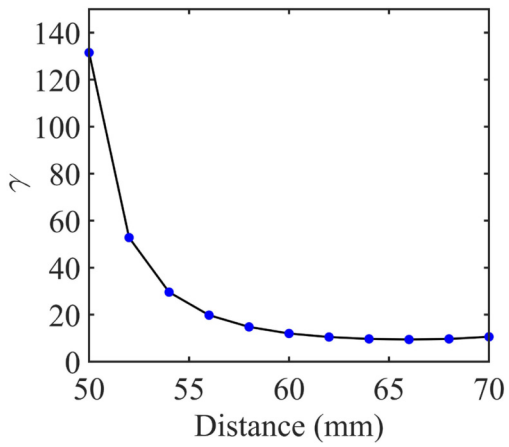

FIG. 12. The variation of γ corresponding to EPs with the distance between the applied forces in the pair.

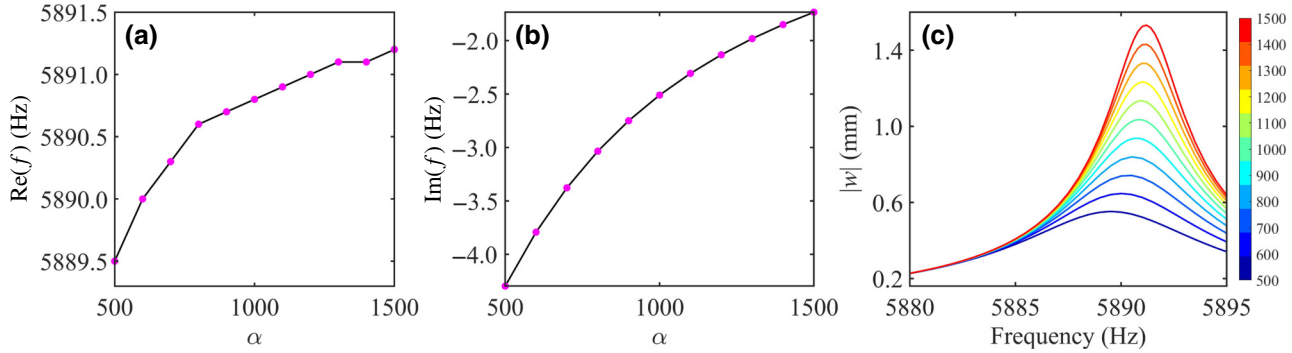

FIG. 13. The variation of the real parts (a) and the imaginary parts (b) of the eigenfrequencies of skin mode 1 with varying α. The magenta points represent the data points and are connected by the black lines. (c) The frequency responses corresponding to the data points. The color scale indicates the values of α.

the results in Fig. 12. One can see that as the distance increases, the γ value of the EP becomes smaller and gradually tends to a stable value. In the main text, we choose the distance 60 mm and the γ value of the EP is 12.

APPENDIX C: INFLUENCE OF DIFFERENT VALUES OF α ON THE SKIN MODE

The skin mode results presented in the main text are all obtained under the condition of $\alpha = 1000$. However, the influence of different values of α on the skin modes needs to be clarified. The eigenfrequencies of skin mode 1 with α varying between 500 and 1500 are calculated and shown in Figs. 13(a) and 13(b). The real parts generally slightly increase with the increase of α, even though there is no obvious law to follow, and the curve connecting the data points fluctuates. As for the imaginary parts, the curve is smooth, and the value monotonically increases as α increases. These variations are reflected in the frequency responses [Fig. 13(c)] showing that with the increase of α, the response peak is gradually enhanced, and the peak frequency slightly shifts to the right. These results indicate that the change of α has a more significant effect on the imaginary parts of the eigenfrequencies compared with the real parts. One can conclude that by changing α, the metabeam constructed in this way still displays the non-Hermitian skin mode, but the resonant frequency and its strength slightly change.

[1] R. El-Ganainy, K. G. Makris, M. Khajavikhan, Z. H. Musslimani, S. Rotter, and D. N. Christodoulides, Non-Hermitian physics and PT symmetry, Nat. Phys. **14**, 11 (2018).
[2] M.-A. Miri and A. Alu, Exceptional points in optics and photonics, Science **363**, eaar7709 (2019).
[3] Y. Ashida, Z. Gong, and M. Ueda, Non-Hermitian physics, Adv. Phys. **69**, 249 (2020).
[4] Z. Gu, H. Gao, P.-C. Cao, T. Liu, X.-F. Zhu, and J. Zhu, Controlling Sound in Non-Hermitian Acoustic Systems, Phys. Rev. Appl. **16**, 057001 (2021).
[5] A. Krasnok, N. Nefedkin, and A. Alu, Parity-time symmetry and exceptional points [Electromagnetic perspectives], IEEE Antennas Propag. Mag. **63**, 110 (2021).
[6] S. Longhi, Parity-time symmetry meets photonics: A new twist in non-Hermitian optics, EPL **120**, 64001 (2018).
[7] C. M. Bender, B. K. Berntson, D. Parker, and E. Samuel, Observation of PT phase transition in a simple mechanical system, Am. J. Phys. **81**, 173 (2013).
[8] C. M. Bender and S. Boettcher, Real Spectra in Non-Hermitian Hamiltonians Having PT Symmetry, Phys. Rev. Lett. **80**, 5243 (1998).
[9] K. Ding, G. Ma, M. Xiao, Z. Zhang, and C. T. Chan, Emergence, Coalescence, and Topological Properties of Multiple Exceptional Points and Their Experimental Realization, Phys. Rev. X **6**, 021007 (2016).
[10] V. Domínguez-Rocha, R. Thevamaran, F. Ellis, and T. Kottos, Environmentally Induced Exceptional Points in Elastodynamics, Phys. Rev. Appl. **13**, 014060 (2020).
[11] M. I. Rosa, M. Mazzotti, and M. Ruzzene, Exceptional points and enhanced sensitivity in PT-symmetric continuous elastic media, J. Mech. Phys. Solids **149**, 104325 (2021).
[12] Y. Liu, Z. Liang, J. Zhu, L. Xia, O. Mondain-Monval, T. Brunet, A. Alù, and J. Li, Willis Metamaterial on a Structured Beam, Phys. Rev. X **9**, 011040 (2019).
[13] Q. Wu, Y. Chen, and G. Huang, Asymmetric scattering of flexural waves in a parity-time symmetric metamaterial beam, J. Acoust. Soc. Am. **146**, 850 (2019).
[14] Z. Lin, H. Ramezani, T. Eichelkraut, T. Kottos, H. Cao, and D. N. Christodoulides, Unidirectional Invisibility Induced by PT-Symmetric Periodic Structures, Phys. Rev. Lett. **106**, 213901 (2011).
[15] X. Zhu, H. Ramezani, C. Shi, J. Zhu, and X. Zhang, PT-Symmetric Acoustics, Phys. Rev. X **4**, 031042 (2014).
[16] R. Fleury, D. Sounas, and A. Alu, An invisible acoustic sensor based on parity-time symmetry, Nat. Commun. **6**, 1 (2015).

[17] D. L. Sounas, R. Fleury, and A. Alù, Unidirectional Cloaking Based on Metasurfaces with Balanced Loss and Gain, Phys. Rev. Appl. **4**, 014005 (2015).

[18] L. Feng, Z. J. Wong, R.-M. Ma, Y. Wang, and X. Zhang, Single-mode laser by parity-time symmetry breaking, Science **346**, 972 (2014).

[19] H. Hodaei, M.-A. Miri, M. Heinrich, D. N. Christodoulides, and M. Khajavikhan, Parity-time–symmetric microring lasers, Science **346**, 975 (2014).

[20] H. Hodaei, A. U. Hassan, S. Wittek, H. Garcia-Gracia, R. El-Ganainy, D. N. Christodoulides, and M. Khajavikhan, Enhanced sensitivity at higher-order exceptional points, Nature **548**, 187 (2017).

[21] X. Fang, N. J. Gerard, Z. Zhou, H. Ding, N. Wang, B. Jia, Y. Deng, X. Wang, Y. Jing, and Y. Li, Observation of higher-order exceptional points in a non-local acoustic metagrating, Commun. Phys. **4**, 1 (2021).

[22] W. Chen, ŞK Özdemir, G. Zhao, J. Wiersig, and L. Yang, Exceptional points enhance sensing in an optical microcavity, Nature **548**, 192 (2017).

[23] P. Djorwe, Y. Pennec, and B. Djafari-Rouhani, Exceptional Point Enhances Sensitivity of Optomechanical Mass Sensors, Phys. Rev. Appl. **12**, 024002 (2019).

[24] X. Zhang, Y. Tian, J.-H. Jiang, M.-H. Lu, and Y.-F. Chen, Observation of higher-order non-Hermitian skin effect, Nat. Commun. **12**, 5377 (2021).

[25] S. Mandal, R. Banerjee, and T. Liew, From the topological spin-Hall effect to the non-Hermitian skin effect in an elliptical micropillar chain, ACS Photonics **9**, 527 (2022).

[26] M. I. Rosa and M. Ruzzene, Dynamics and topology of non-Hermitian elastic lattices with non-local feedback control interactions, New J. Phys. **22**, 053004 (2020).

[27] C. H. Lee, L. Li, and J. Gong, Hybrid Higher-Order Skin-Topological Modes in Nonreciprocal Systems, Phys. Rev. Lett. **123**, 016805 (2019).

[28] M. Brandenbourger, X. Locsin, E. Lerner, and C. Coulais, Non-reciprocal robotic metamaterials, Nat. Commun. **10**, 1 (2019).

[29] P. Gao, M. Willatzen, and J. Christensen, Anomalous Topological Edge States in Non-Hermitian Piezophononic Media, Phys. Rev. Lett. **125**, 206402 (2020).

[30] C. H. Lee and R. Thomale, Anatomy of Skin Modes and Topology in Non-Hermitian Systems, Phys. Rev. B **99**, 201103 (2019).

[31] Y.-X. Xiao and C. Chan, Topology in Non-Hermitian Chern Insulators with Skin Effect, Phys. Rev. B **105**, 075128 (2022).

[32] C. Scheibner, W. T. Irvine, and V. Vitelli, Non-Hermitian Band Topology and Skin Modes in Active Elastic Media, Phys. Rev. Lett. **125**, 118001 (2020).

[33] D. Braghini, L. G. Villani, M. I. Rosa, and J. R. de F Arruda, Non-Hermitian elastic waveguides with piezoelectric feedback actuation: Non-reciprocal bands and skin modes, J. Phys. D: Appl. Phys. **54**, 285302 (2021).

[34] Z. Hou and B. Assouar, Tunable elastic parity-time symmetric structure based on the shunted piezoelectric materials, J. Appl. Phys. **123**, 085101 (2018).

[35] M. Farhat, P.-Y. Chen, S. Guenneau, and Y. Wu, Self-Dual Singularity through Lasing and Antilasing in Thin Elastic Plates, Phys. Rev. B **103**, 134101 (2021).

[36] D. Li, S. Huang, Y. Cheng, and Y. Li, Compact asymmetric sound absorber at the exceptional point, Sci. China: Phys., Mech. Astron. **64**, 1 (2021).

[37] X. Wang, X. Fang, D. Mao, Y. Jing, and Y. Li, Extremely Asymmetrical Acoustic Metasurface Mirror at the Exceptional Point, Phys. Rev. Lett. **123**, 214302 (2019).

[38] Y. Jin, B. Djafari-Rouhani, and D. Torrent, Gradient index phononic crystals and metamaterials, Nanophotonics **8**, 685 (2019).

[39] Y. Jin, L. He, Z. Wen, B. Mortazavi, H. Guo, D. Torrent, B. Djafari-Rouhani, T. Rabczuk, X. Zhuang, and Y. Li, Intelligent on-demand design of phononic metamaterials, Nanophotonics **11**, 439 (2022).

[40] L. He, Z. Wen, Y. Jin, D. Torrent, X. Zhuang, and T. Rabczuk, Inverse design of topological metaplates for flexural waves with machine learning, Mater. Des. **199**, 109390 (2021).

[41] Y. Jin, Y. Pennec, B. Bonello, H. Honarvar, L. Dobrzynski, B. Djafari-Rouhani, and M. I. Hussein, Physics of surface vibrational resonances: pillared phononic crystals, metamaterials, and metasurfaces, Rep. Prog. Phys. **84**, 086502 (2021).

[42] See Supplemental Material at http://link.aps.org/supplemental/10.1103/PhysRevApplied.18.014067 for details, including I. eigenfrequencies and mode shapes of the lower EP, II. EP in other types of metabeam, III. relationship between the model parameters and EP, IV. realizing EP using piezoelectric elements, V. realizing skin mode using piezoelectric elements, VI. influence of global loss on EP and skin mode, and VII. output power comparison.

[43] Y. Zhu and L. Zhu, Accessing the exceptional points in coupled Fabry–Perot resonators through hybrid integration, ACS Photonics **5**, 4920 (2018).

[44] Z. Gu, H. Gao, T. Liu, S. Liang, S. An, Y. Li, and J. Zhu, Topologically Protected Exceptional Point with Local Non-Hermitian Modulation in an Acoustic Crystal, Phys. Rev. Appl. **15**, 014025 (2021).

[45] T. T. Koutserimpas and R. Fleury, Nonreciprocal Gain in Non-Hermitian Time-Floquet Systems, Phys. Rev. Lett. **120**, 087401 (2018).

[46] C. Coulais, D. Sounas, and A. Alu, Static non-reciprocity in mechanical metamaterials, Nature **542**, 461 (2017).

[47] D. L. Sounas and A. Alu, Non-reciprocal photonics based on time modulation, Nat. Photonics **11**, 774 (2017).

[48] Z. Wen, Y. Jin, P. Gao, X. Zhuang, T. Rabczuk, and B. Djafari-Rouhani, Topological cavities in phononic plates for robust energy harvesting, Mech. Syst. Signal Proc. **162**, 108047 (2022).

[49] Z. Wen, W. Wang, A. Khelif, B. Djafari-Rouhani, and Y. Jin, A perspective on elastic metastructures for energy harvesting, Appl. Phys. Lett. **120**, 020501 (2022).

[50] E. Rivet, A. Brandstötter, K. G. Makris, H. Lissek, S. Rotter, and R. Fleury, Constant-pressure sound waves in non-Hermitian disordered media, Nat. Phys. **14**, 942 (2018).

[51] R. Fleury, D. L. Sounas, C. F. Sieck, M. R. Haberman, and A. Alù, Sound isolation and giant linear nonreciprocity in a compact acoustic circulator, Science **343**, 516 (2014).

[52] Z. Wen, S. Zeng, D. Wang, Y. Jin, and B. Djafari-Rouhani, Robust edge states of subwavelength chiral phononic plates, Extreme Mech. Lett. **44**, 101209 (2021).

[53] M. Hwang and A. F. Arrieta, Input-independent energy harvesting in bistable lattices from transition waves, Sci. Rep. **8**, 1 (2018).

[54] S. Gonella, A. C. To, and W. K. Liu, Interplay between phononic bandgaps and piezoelectric microstructures for energy harvesting, J. Mech. Phys. Solids **57**, 621 (2009).

[55] W. Wang, J. Iglesias, Y. Jin, B. Djafari-Rouhani, and A. Khelif, Experimental realization of a pillared metasurface for flexural wave focusing, APL Mater. **9**, 051125 (2021).

[56] Y. Jin, W. Wang, Z. Wen, D. Torrent, and B. Djafari-Rouhani, Topological states in twisted pillared phononic plates, Extreme Mech. Lett. **39**, 100777 (2020).

[57] H. Nassar, H. Chen, A. Norris, and G. Huang, Nonreciprocal flexural wave propagation in a modulated metabeam, Extreme Mech. Lett. **15**, 97 (2017).

[58] R. Cai, Y. Jin, T. Rabczuk, X. Zhuang, and B. Djafari-Rouhani, Propagation and attenuation of Rayleigh and pseudo surface waves in viscoelastic metamaterials, J. Appl. Phys. **129**, 124903 (2021).